https://doi.org/10.1016/j.apenergy.2019.01.025

Thermal modelling of ethanol-fuelled Solid Oxide Fuel Cells

Bin Chen[1,2], Haoran Xu[2], Peng Tan[2,3], Yuan Zhang[2,4], Xiaoming Xu[2,5], Weizi Cai[2], Meina Chen[2,6], Meng Ni[2,*]

[1] Institute of Deep Earth Science and Green Energy, Shenzhen University, Shenzhen 518060, China
[2] Building Energy Research Group, Department of Building and Real Estate, The Hong Kong Polytechnic University, Hung Hom, Kowloon, Hong Kong, China
[3] Department of Thermal Science and Energy Engineering, University of Science and Technology of China, Hefei, 230026, China
[4] State Key Laboratory of Materials-Oriented Chemical Engineering, College of Chemical Engineering, Nanjing Tech University, Nanjing 210009, China
[5] School of Automotive and Traffic Engineering, Jiangsu University, Zhenjiang 212013, China
[6] School of Physics and Electronics, Shandong Normal University No.88 Wenhua Dong Road, Lixia District, Jinan, Shandong Province, 250014, China

[*] Corresponding author: Email: meng.ni@polyu.edu.hk

Tel: 852-27664152; Fax: 852-27645131

Abstract

A 2D thermal model is developed to investigate an ethanol-fuelled Solid Oxide Fuel Cells with a Ni-ZrO_2/CeO_2 functional layer for internal reforming of ethanol. The catalytic kinetics of the functional layer used in this model is validated in terms of ethanol conversion and product selectivity in the experimental data of a fixed-bed testing reactor. The simulated E-SOFC demonstrates typical performance of 4385.6 A m^{-2} at 0.6 V, corresponding to a power density of 2631.4 W m^{-2}, with a high conversion ratio of ethanol (0.903) at 700ºC. Parametric studies of voltage, water to ethanol ratio and inlet fuel gas temperature are conducted and comprehensively analysed, concluding that the positive effects of lowering the voltage and increasing the inlet temperature on the ethanol conversion. We find that adding the reforming layer is a facile and effective way to replace the conventional H_2 by abundant-in-nature ethanol for SOFC from the numerical analysis. Attention is also drawn to the carbon deposition risk by thermodynamic analysis of the gas composition, suggesting to keep the water to ethanol ratio higher than 3. The as-developed model can serve as an effective tool for the optimization of the operating conditions and geometry design to avoid carbon deposition and improve performance of ethanol-fuelled Solid Oxide Fuel Cells.

Keywords: Internal reforming; Numerical modelling; Solid oxide fuel cells; Ethanol.

1. Introduction

Solid oxide fuel cells (SOFCs) are high temperature fuel-to-power devices [1,2]. The high operating temperature (500−900°C) enables SOFCs to directly use hydrocarbons [3], including hydrogen, syngas, methane, ethanol [4], propane, ammonia [5,6], reformed urea [7], carbon [8], etc. for power generation. Among those fuels, ethanol possesses many attractive physicochemical properties and features, including its high energy density, easiness of transportation and storage. Moreover, ethanol can be produced from renewable biomass such as wheat cellulose [9], crop [10] and algal [11]. Therefore, it is attracting intensive research attention to develop SOFC running on renewable bio-ethanol by internal reforming using steam as the reforming agent:

$$C_2H_5OH + 3H_2O \rightarrow 2CO_2 + 6H_2 \;\; \Delta H^0_{298K} = 173.5 \text{ kJ mol}^{-1} \quad (1)$$

Conventionally, ethanol steam reforming reaction (**Eq. 1**) is a cheap and efficient method to produce hydrogen, which is thermodynamically favoured when the reforming temperature is higher than 500 K at ambient pressure. Therefore, it can be internally implemented in ethanol-fuelled SOFC (E-SOFC) to achieve efficient and carbon-neutral power generation if the ethanol is from renewable sources. In this respect, the E-SOFC can be more promising than the common hydrogen-fuelled SOFC, for which hydrogen production is usually energy intensive, such as water electrolysis and coal gasification. Moreover, the internal reforming of ethanol can be promoted by the *in-situ* consumption of H_2 and CO according to the Le Chatelier's principle, leading to high energy efficiency and system compactness compared to external-reformed ethanol-fuelled SOFC [12].

Albeit ethanol conversion is thermodynamically high at typical working temperatures of SOFC, the E-SOFC still has various issues to be investigated regarding the reforming process at the anode side. For example, the highly endothermic nature of **Eq. 1** tends to lower the E-SOFC temperature, which in turn decreases the cell performance, including electrochemical activity, material degradation due to temperature gradient and thermal expansion mismatch, etc. Additionally, the carbon deposition issue and energy efficiency degrading of E-SOFC depend on the steam reforming rate of ethanol and the temperature distribution. Therefore, research efforts are needed for the careful management of the steam reforming process, especially its thermal integration with the electrochemical processes in E-SOFC. Although thermodynamic analyses on ethanol-fueled SOFC are available, no numerical study focusing on the detailed electrochemical reaction, chemical reaction and heat mass transfer processes

has been conducted. It should be noted that the detailed electrochemical-thermal modelling of the E-SOFC is essential for understanding the various processes in the cell and for optimizing the operating conditions for performance improvement.

In this work, we developed a multi-physical thermal model for a tubular E-SOFC with a 40 μm thick functional layer on the inner surface of Ni/YSZ anode support for ethanol steam reforming. The focus of the simulation is on the thermal integration of the endothermic ethanol steam reforming and exothermic electrochemical reactions. The ethanol conversion and co-electrochemical oxidation of the CO and H_2 in E-SOFC are evaluated in detail. Critical operating conditions (voltage, water to ethanol ratio and inlet flow temperature) are investigated to identity their influence on the E-SOFC performance.

2. Ethanol-fuelled SOFC design and model development

The reaction pathway of overall ethanol steam reforming above 350°C is represented by sub reactions including the water gas shifting (WGSR) and methane stream reforming reactions (MSR), following the ethanol decomposition (EDR) on catalytic sites of metal initiated by the dissociation of C-C bond [13−15]:

$$C_2H_5OH \rightarrow CH_4 + CO + H_2 \quad \Delta H^0_{298K} = 49 \text{ kJ mol}^{-1} \tag{2}$$

$$CO + H_2O \rightarrow CO_2 + H_2 \quad \Delta H^0_{298K} = -41 \text{ kJ mol}^{-1} \tag{3}$$

$$CH_4 + H_2O \rightarrow CO + 3H_2 \quad \Delta H^0_{298K} = 206 \text{ kJ mol}^{-1} \tag{4}$$

Therefore the kinetics of the aforementioned three sub reactions can be adopted to describe the overall kinetics of the ethanol steam reforming in this study. As the carbon deposition issue is detrimental to the durability of the Ni-based catalyst via surface deactivation, supporting materials (aluminium oxide, ceria and zirconia, etc.) are usually employed as the Ni particle support. The supporting material can optimize the Ni dispersion, reduce the sintering of Ni and promote the carbon removal due to its high oxygen mobility on surface [16,17]. Here in this study, the most commonly used Ni-loaded (30 wt.%) CeO_2/ZrO_2 catalyst is employed to form a functional layer for ethanol reforming. A kinetic model is available for ethanol reforming, based on a comprehensive experimental testing at temperature 600−700°C [18]. The dimensional design of the ethanol reforming layer implemented SOFC is schemed in **Fig. 1** with details being summarized in **Table 1**.

2.1 Electrochemical model

Conventional SOFC materials are used in this numerical study for the tubular SOFC as shown in **Table 1**. The electrochemical model are already well developed in our previous works [22,23] based on a secondary current distribution framework. The conduction of positively charged oxygen ion and negatively charged electron are modelled separately and linked by equilibrium potential of interfacial electrochemical reactions and activation overpotentials. The following will briefly list the model details. Nernst equations for H_2 and CO electrochemical oxidation are employed to determine their temperature-dependent equilibrium potentials, considering the local concentration loss (**Eq. 5−6**):

$$E_{H_2} = 1.253 - 0.00024516T + \frac{RT}{2F} ln\left[\frac{P_{H_2}(P_{O_2})^{0.5}}{P_{H_2O}}\right] \quad (5)$$

$$E_{CO} = 1.467 - 0.0004527T + \frac{RT}{2F} ln\left[\frac{P_{CO}(P_{O_2})^{0.5}}{P_{CO_2}}\right] \quad (6)$$

, that should both comply the potential balance with the difference between the ion conducting phase and electron conducting phasing. Take the anode side as example:

$$\emptyset_l - \emptyset_s = E_{H_2/CO} - \eta_{act.a} \quad (7)$$

The η_{act} is the activation overpotential of electrochemical reactions, that can be linked to the local current densities of H_2 and CO oxidation currents ($i_{source.a_{H2}}$ or $i_{source.a_{CO}}$) by the classic Butler-Volmer equation for the anode, as well as the oxygen reduction current for the cathode ($i_{source.c}$):

$$i_{source.a_{H2/CO}} = AV_a \cdot i_{o.a_{H2/CO}} \left(exp\left(\frac{2F \cdot \eta_{act.a}}{RT}\right) - \frac{p_{H_2/CO}}{p_{H_2/CO.ref}} exp\left(\frac{-2F \cdot \eta_{act.a}}{RT}\right)\right) \quad (8)$$

$$i_{source.c} = AV_c \cdot i_{o.c} \left(\frac{p_{H_2O}}{p_{H_2O.ref}} exp\left(\frac{2F \cdot \eta_{act.c}}{RT}\right) - \frac{p_{O_2}}{p_{O_2.ref}} exp\left(\frac{-2F \cdot \eta_{act.c}}{RT}\right)\right) \quad (9)$$

The $i_{o.c}$ and $i_{o.a_{H2/CO}}$ represent the values of the cathodic exchange current density and the anodic exchange current densities [24]. The AV_a is defined as the specific active area of the anode (2.33×10^5 in unit of $m^2\ m^{-3}$) and the cathode AV_c as $2.46\times10^5\ m^{-1}$ for [25,26]. The charge conduction is modelled by the electron conduction in Ni and LSM and the oxygen ion conduction in YSZ, respectively:

$$i_l = -\sigma_{l.eff} \nabla(\emptyset_l),\ \nabla i_l = Q_l + i_{source} \quad (10)$$

$$i_s = -\sigma_{s.eff} \nabla(\emptyset_s),\ \nabla i_s = Q_s - i_{source} \quad (11)$$

, where the effective conductivity of oxygen ion conductivity ($\sigma_{l.eff}$) and electron conductivity($\sigma_{s.eff}$) can be computed by the electrode intrinsic conductivity, tortuosity and porosity [23].

2.2 Heat transport model

It is necessary to carefully model the heat transport process in both the porous media and the channel, as the chemical and electrochemical processes could significantly affect the temperature field. In this work, the heat transfer in both the porous media and the channels can be modelled using the following general energy conservation equation:

$$\left(\rho c_p\right)_{eff} U \cdot \nabla T + \nabla\left(-\lambda_{eff} \nabla T\right) = Q_{heat} \tag{12}$$

, where the "*eff*" subscript denotes the effective thermodynamic properties, including the density, heat capacity and heat conductivity by fraction averaging:

$$\left(\rho c_p\right)_{eff} = \varepsilon \rho_g c_{p.g} + (1-\varepsilon)\rho_s c_{p.s} \tag{13}$$

$$\lambda_{eff} = \varepsilon \lambda_g + (1-\varepsilon)\lambda_s \tag{14}$$

The heat source term (Q_{heat}) includes reaction enthalpy change of WGSR, MSR and EDR as ascribed by **Eq. (2−3)**. The calculation of those reaction rates are described in the next section. Additional electrochemical heat sources are considered in the electrodes and electrolyte, including the electrochemical reaction heat and heat due to overpotential losses.

2.3 Mass and momentum transport model

The reaction rate of ethanol decomposition reaction follows a simple mass-action type kinetics below that is sufficient to simulate the behaviour under operating conditions:

$$R_{EDR} = K_{EDR} P_e \tag{15}$$

$$K_{EDR} = 8E6 \times exp\left(-\frac{E_{EDR}}{RT}\right) \ [mol\ s^{-1}\ m^{-3}] \tag{16}$$

, where the E_{EDR} is 64.8 kJ mol^{-1} [13] and the P_e represents partial pressure of ethanol. Regarding the WGSR and MSR, kinetics expressions over Ni active sites [27,28] are verified by tuning the pre-exponential coefficient to fit experimental data:

$$R_{WGSR} = K_{sf}\left(p_{H_2O} p_{CO} - \frac{p_{H_2} p_{CO_2}}{K_{ps}}\right)(mol\ m^{-3} s^{-1}) \tag{17}$$

$$K_{sf} = 0.0171\, exp\left(\frac{-103191}{RT}\right)\ (mol\, m^{-3} Pa^{-2} s^{-1}) \quad (18)$$

$$K_{ps} = exp(-0.2935Z^3 + 0.6351Z^2 + 4.1788Z + 0.3169) \quad (19)$$

$$R_{MSR} = K_{rf}\left(p_{CH_4} p_{H_2O} - \frac{p_{H_2}(p_{H_2})^3}{K_{pr}}\right)(mol\, m^{-3} s^{-1}) \quad (20)$$

$$K_{rf} = 2395\, exp\left(\frac{-231266}{RT}\right)\ (mol\, m^{-3} Pa^{-2} s^{-1}) \quad (21)$$

$$\mathrm{K_{pr}} = 1.0267 \times 10^{10} \exp\left(-0.2513\mathrm{Z}^4 + 0.3665\mathrm{Z}^3 + 0.581\mathrm{Z}^2 - 27.134\mathrm{Z} + 3.277\right) \quad (22)$$

$$Z = \frac{1000}{T(K)} - 1 \quad (23)$$

The aforementioned kinetic expressions are implemented in the mass conservation equations as the source terms at the right hand side:

$$\nabla \cdot (\rho U) = \sum \mathrm{M}_i R_i \quad (24)$$

$$\nabla\left(-\rho \cdot w_i \sum_{j \neq i}^{n} (D_{eff,ij}\, (\nabla x_j + (x_j - w_j) \cdot \nabla P \cdot P^{-1}))\right) + \rho(U \cdot \nabla) w_i = R_i \quad (25)$$

The $D_{eff,ij}$ is binary effective diffusion coefficient [29] of species i and j. The mole fraction and mass fraction of species j are defined as x_j and w_j. The gas density (ρ) is calculated by the volume-averaged density of species as an ideal gas mixture.

The momentum transport equation of the gas flow in porous electrodes is formulated as:

$$\frac{\rho}{\varepsilon}\left((U \cdot \nabla)\frac{U}{\varepsilon}\right) = \nabla \cdot \left[-p + \frac{\mu}{\varepsilon}(\nabla U + (\nabla U)^T) - \frac{2}{3}\frac{\mu}{\varepsilon}(\nabla \cdot U)\right] - \mu\kappa^{-1} U \quad (26)$$

, where κ is the permeability and μ is the dynamic viscosity. The value of ε (porosity) in non-porous channel, is set to be 1 and the $\mu\kappa^{-1}U$ term is cancelled.

The aforementioned models are developed in a Finite Element Method based computational fluid dynamics simulation platform COMSOL v5.2. The simulated geometry model is discretized by 28100 structured Quad elements with 274466 degrees of freedom. The meshing of the model is fine enough to guarantee the mesh independence. More detailed boundary conditions can be found in **Table 3**.

2.4 Model Validation

To validate the catalyst reforming activity, four reforming indicators are measured and compared with experimental results of a fixed-bed reactor [18]:

$$\text{Ethanol conversion} = \frac{F_{ethanol,in} - F_{ethanol,out}}{F_{ethanol,in}} \times 100\% \quad (27)$$

$$H_2 \text{ selectivity} = \frac{F_{H2,out}}{F_{H2,out} + F_{CO,out} + F_{CO2,out} + F_{CH4,out}} \times 100\% \quad (28)$$

$$\text{CO selectivity} = \frac{F_{CO,out}}{F_{H2,out} + F_{CO,out} + F_{CO2,out} + F_{CH4,out}} \times 100\% \quad (29)$$

$$CO_2 \text{ selectivity} = \frac{F_{CO2,out}}{F_{H2,out} + F_{CO,out} + F_{CO2,out} + F_{CH4,out}} \times 100\% \quad (30)$$

$$CH_4 \text{ selectivity} = \frac{F_{CH4,out}}{F_{H2,out} + F_{CO,out} + F_{CO2,out} + F_{CH4,out}} \times 100\% \quad (31)$$

, of which the flowrates at the outlet of both gas and liquid species were measured by gas chromatographs. The dimensions and operating conditions of the fixed-bed reactor is summarized in **Table 2**. The bed is also simulated on the FEM platform COMSOL v5.2 as a 2D isothermal porous flow, assuming that the flow gas behaves as the ideal gas at operating temperature of 600−700°C. The good agreement shown in **Fig. 2b−2c** verifies the good accuracy of the adopted reforming kinetic to be used in the reforming layer. Regarding the electrochemical model, the validation can be referred to our previous work [28], where the same model and same SOFC design as this work were adopted and well validated by comparing with the experimental results both in SOFC and SOEC operation modes (Fig. 3 of ref. [28]).

3. Results and Discussion

3.1 Base case analysis

The E-SOFC is operated at the base case condition as specified in **Table 1** to demonstrate the interaction between ethanol reforming and SOFC. **Fig. 3a** shows the cross-sectional temperature distribution of the four-layered MEA component (reforming layer, anode, cathode and electrolyte), enclosed by the anode channel and cathode channel.

It can be seen that the temperature of both anode and cathode flow gradually increases along the flow streams, indicating that the cooling effect of endothermic reforming can be mitigated. This mitigation results from simultaneous heat sources associated with the water gas shifting reaction as evidenced by **Fig. 3b** that the R_{WGSR} is of the same magnitude as R_{EDR}. It is also largely contributed by the electrochemical heat generation at 0.6 V. **Fig. 3c−3e** shows the reaction rate distribution at the anode side (reforming layer and the support layer). We assign 0 to the anode channel and the figures are scaled to show the results more clearly. As shown

in **Fig. 3b**, the WGSR is mainly concentrated in the reforming layer, as it is kinetically more active than ethanol decomposition and the latter produces CO in the reforming layer as the reactant for the WGSR.

It can be observed that the value of R_{WGSR} becomes negative at the region close to the anode-electrolyte interface, especially at the downstream. This observation can be simply explained by the increased fraction ratio of CO_2:CO close to the interface due to the CO electroreduction current, as evidenced by the separated current sources at different distances to the anode-electrolyte interface profiled in **Fig. 4a** and the species fraction distribution in **Fig. 4b**. On account of the H_2 electrochemical oxidation favours the water gas shifting to generate H_2, the negative R_{WGSR} as-observed points out that the water gas shifting reaction is more thermodynamically sensitive to the CO and CO_2 fractions than the H_2 and H_2O fraction. It can be explained by the H_2 and H_2O are quite abundant in this case. Different from R_{WGSR}, R_{MSR} is relatively uniform in the reforming layer and the magnitude of R_{MSR} in the reforming layer is relatively lower than R_{EDR}. Since the R_{MSR} in the anode support also contributes to the consumption of CH_4 produced from EDR and its magnitude is well-maintained along the flow due to the increase of temperature, the fraction of CH_4 is still at a low level (close to 0) at the anode electrolyte interface as seen from **Fig. 4b** and **Fig. 4c.**

Overall, the E-SOFC achieves a power output of 2631.4 W m^{-2}, corresponding to an average current density of 4385.6 A m^{-2} as summarized in **Table 4**. The conversion of ethanol can reach 0.903 with 72.75 vol% H_2O at the outlet due to the electrochemical reaction and chemical reactions (**Fig. 4b**). The predicted composition profile indicates that the carbon deposition can be potentially refrained in the SOFC-integrated ethanol steam reforming, benefitting from the high level of H/C ratio along the reacting flow [30].

3.2 Effects of operating voltage

To examine the effects of operating voltage on the performance of E-SOFC, the current density of the cell is simulated at voltage from 0.8 V to 0.35 V. **Fig. 5a** shows that the increase of voltage facilitate the ethanol conversion (reaches >0.9 when the operating voltage lower than 0.6 V). The observed improvement can be ascribed to two reasons: (1) in the case of high current operation, the fast conversion of CO and H_2 products in the electrochemically active region, beneath the reforming layer at the vicinity of anode-electrolyte interface of E-SOFC, would help to reduce the concentration of reforming products; (2) the lower operating voltage leads to large overpotential heat generation in the MEA assembly. Therefore the as-

expected temperature increase (**Fig. 5c**) favours the deep conversion of ethanol from the thermodynamic viewpoint. Accordingly, the selectivity of other species in **Fig. 5a** changes (H_2 and CO decreases, while CO_2 increases) because the consumption of H_2 and CO by the SOFC is enhanced at lower operating voltage.

Fig. 6 provides the reaction rate distributions at V=0.4, 0.6 and 0.8 V. All the R_{WGSR}, R_{MSR} and R_{ESR} are enhanced at the lower voltage. Again, negative WGSR close to the anode-electrolyte is found and becomes more obvious in the case of lower voltage operation. This should be explained by the faster conversion of CO at lower voltage.

3.3 Effects of water to ethanol ratio

Albeit the E-SOFC running on dry ethanol is promising as demonstrated by experimental works [31−33], the coking issue still remains. Currently there are several solutions for this issue, including optimizing the dispersion of active sites [33]; casting functioning layer over the anode [3,34]; using water absorbable anode support [17,30]; introduction of partial oxidation of ethanol [35], etc. One simple and effective method is to introduce water steam to facilitate the reforming of ethanol, thus reducing the coking issue of hydrocarbon-fuelled SOFC [32].

The participation of water in E-SOFC is critical to both the ethanol reforming and electrochemical reactions. Therefore, the effects of the addition amount of water steam are investigated in this section by changing the water to ethanol feeding ratio R_{WE} from 3 (stoichiometric reforming) to 8. As seen from **Fig.7a**, the linear correlation between the ethanol conversion and R_{WE} is observed at 3 different feeding flowrates of ethanol and the lower R_{WE} results in a higher conversion of ethanol as a result of the reduced R_{EDR} (**Fig. 8c**). This indicates the dilution effects of excessive H_2O can be the rate-determining effect for the EDR in the E-SOFC. The dilution effect also leads to the drop of current density (also power density) value at higher R_{WE} and feeding flow rate in **Fig. 7b**. Comparing the selectivity of CO and H_2 in **Fig. 7c1−c2**, the opposite trends of CO and H_2 could be caused by the equilibrium shifting of WGSR due to the introduction of large amount of H_2O. The reaction rate distribution of WGSR in Fig. 8a verifies this guess by the lower magnitude of R_{WGSR} at R_{WE}=8 than R_{WE}=4 case. As a result of the shifting, the CO_2 fraction is also improved (**Fig. 7c4**), although the electrochemical conversion of CO to CO_2 is reduced. The temperature distribution is shown in Fig. 8d and again can account for the decrease of current density due to the cooling, originating from the dilution effects of excessive feeding of H_2O.

It can be concluded from this effect study that the increase of H_2O addition compromises the electrochemical performance, while benefiting the output H_2 content if the E-SOFC is considered more as a reformer, serving for the cogeneration of H_2 and power. Another drawback of using an excessive amount of water steam (large R_{WE}) is the parasitic energy cost of water vaporization. Therefore in practice, determination of the H_2O amount to be mixed with ethanol, might be a critical concern of developers in finding the trading-off point between the durability and efficiency. The simulated fuel gas composition trajectory from inlet to outlet is a straightforward indicator that helps developers to quantify the risk of carbon formation as thermodynamically regionalized in **Fig. 9** at any positions of the flow. Taking 100 K as the safe temperature difference allowed for the actual temperature at a particular position (T_{actual}) and the critical deposition temperature (T_c) at that position, it can be suggested that the R_{WE} should be over 3 to make T_{actual}-T_c>100 K. The increasing of R_{WE} to 6 can effectively deviate the composition away from the deposition boundary of 973 K (solid black line). We can also infer that at the starting-up stage, the inlet part of the SOFC is more vulnerable to carbon deposition as the temperature may not be high enough.

3.4 Effects of inlet flow temperature

The temperature of the inlet fuel and air has a great impact on the rates of all involved reforming reactions and the electrochemical performance of the SOFC. Simulations are conducted with the inlet temperature being increased from 873 K to 1073 K. **Fig. 10a** clearly presents the greatly enhanced current and power density due to the rise in temperature at different R_{WE} cases. It suggests a synergistic promotion effect between the temperature and the current density as shown in **Fig. 10b** that the higher current density operation would lead to an enhanced temperature increase along the flow direction, by means of associated electrochemical heating.

Fig. 11a−c demonstrates the positive effect of temperature on the ethanol conversion, however, the selectivity of H_2 at the outlet is reduced due to the enhanced conversion of H_2 to H_2O although the R_{WGSR} is enhanced at higher temperature (**Fig. 11d**). Also, the greatly improved high selectivity of CO_2 (red dotted line) implies that the increase of operating temperature can effectively improve the hydrocarbon fuel utilization by promoting the conversion of ethanol and methane to CO and H_2 for direct utilization in SOFC. To account for this statement, the change of R_{MSR} and R_{EDR} in **Fig. 11e−f** both exhibits the quicker completion of the conversion of ethanol and methane at higher inlet temperature, as observed from the peak-shaped reaction rate profile along the flow.

4. Discussion

The direct fuelling of ethanol to SOFC highlights the advantages of utilizing renewable bio-ethanol in a clean and efficient way. Currently, other types of fuel cells also can also use ethanol fuel for power generation, such as direct alkaline ethanol fuel cell (DEFC), which works at room temperature instead and is under intensive research [36,37].

It is reported that the biggest challenge to DEFC performance is the kinetically sluggish direct oxidation of ethanol electrochemical (EOR) [36]. As a result, the anode side of DEFC, where EOR occurs, still requires noble catalysts (Pt, Pd, etc.), and the power density of DEFC is still usually lower than that of E-SOFCs as seen from the comparison of the power density of DEFC [37−47] and E-SOFC from literatures [34,48−64] in **Fig. 12**. It hinders the application of DEFC in large scale energy generation scenarios such as grid stabilization, distributed power generation. On the other hand, E-SOFC has higher power density (up to the level of 1 W cm^{-2}), but higher system complexity, so that the balance of plant (BOP) should be provided for maintaining a suitable thermal condition for the SOFC stack, as well as recovering waste heat by peripheral components, such as water/ethanol evaporators and heat exchangers. In this regard, E-SOFC could be more advantageous than DEFC for stationary applications in agricultural districts where bio-ethanol is usually resourceful, while the DEFC is attractive in small-scale/residential applications where the attended operation of the fuel cell stack is unpractical.

5. Conclusions

To this end, we can conclude from the numerical results that the ethanol-fuelled SOFC achieves a typical performance of 4385.6 A m^{-2} and 2631.4 W m^{-2} at 0.6 V, 700ºC, with a high conversion of ethanol (0.903). The endothermic effects of reforming reactions are effectively mitigated by the *in-situ* generated electrochemical heat. Parametric studies show that firstly, lowering the operating voltage can further improve the conversion of ethanol, however concentration overpotential will be worse, as long as the voltage is lower than 0.5 V. The mutual enhancing effect between voltage lowering and temperature increase is clearly observed from the results of voltage parametric study and evidenced by the enhanced R_{WGSR}, R_{MSR} and R_{ESR}; Secondly, the change of inlet water to ethanol ratio is a critical parameter to the current-power performance of the SOFC, while should be kept over 3, measured by the risk of carbon deposition formation observed from the ternary diagram. Additional caution for carbon deposition should be paid to the inlet part of the SOFC. Finally, the increase of

inlet temperature is proved to be beneficial for both the ethanol utilization and the current-power performance through the synergistic effect from the promotion of temperature and the current density.

Future works on ethanol-fuelled SOFC may be directed to the introduction of partial oxidation to the anode fuel so as to mitigate the temperature gradient of tubular SOFC. Material research should be devoted to the development of effective reforming layer with better compatibility with the anode support layer.in terms of chemical, mechanical matching.

Overall, the developed numerical model provides insight of the composition evolution inside the SOFC, that is influenced by the coupled reforming process and electrochemical oxidation of CO and H_2, which is heuristic to future design and optimization of ethanol-fuelled SOFC.

Acknowledgements

This research was supported by grants from Research Grant Council, University Grants Committee, Hong Kong SAR. (Project Number: PolyU 152214/17E) and the National Natural Science Foundation of China (Grant No.51602183).

References

[1] O'hayre R, Cha S-W, Prinz FB, Colella W. Fuel cell fundamentals. John Wiley & Sons; 2016.

[2] Zhang Y, Knibbe R, Sunarso J, Zhong Y, Zhou W, Shao Z, Zhu Z. Recent Progress on Advanced Materials for Solid-Oxide Fuel Cells Operating Below 500°C, Adv Mater 2017;29:1700132.

[3] Lo Faro M, Antonucci V, Antonucci PL, Aricò AS. Fuel flexibility: A key challenge for SOFC technology. Fuel 2012;102:554–9.

[4] Laosiripojana N, Assabumrungrat S. Catalytic steam reforming of methane, methanol and ethanol over Ni/YSZ: The possible use of these fuels in internal reforming SOFC. J Power Sources2007;163:943–51.

[5] Lan R, Irvine JTS, Tao S. Ammonia and related chemicals as potential indirect hydrogen storage materials. Int J Hydrogen Energy 2012;37:1482–94.

[6] Perna A, Minutillo M, Jannelli E, Cigolotti V, Nam SW, Han J. Design and performance assessment of a combined heat, hydrogen and power (CHHP) system based on ammonia-fueled SOFC, Appl Energy 2018;231:1216–1229.

[7] Cinti G, Desideri U. SOFC fuelled with reformed urea. Appl Energy. 2015; 154:242–253.

[6] Cao D, Sun Y, Wang G. Direct carbon fuel cell: fundamentals and recent developments. J Power Sources 2007;167:250–7.

[9] Xu Y, Wang D, Integrating starchy substrate into cellulosic ethanol production to boost ethanol titers and yields. Appl Energy 2017;195:196–203.

[10] Chen X, Khanna M. Effect of corn ethanol production on Conservation Reserve Program acres in the US. Appl Energy. 2018;225:124–134.

[7] Baeyens J, Kang Q, Appels L, Dewil R, Lv Y, Tan T. Challenges and opportunities in

improving the production of bio-ethanol. Prog Energy Combust Sci 2015;47:60–88.
[8] Tippawan P, Arpornwichanop A. Energy and exergy analysis of an ethanol reforming process for solid oxide fuel cell applications. Bioresour Technol 2014;157:231–9.
[9] Divins NJ, Schbib S, Borio D, Lo E. Ethanol steam reforming for hydrogen generation over structured catalysts. Int J Hydrogen Energy 2013;38:4418–28.
[10] Idriss H, Scott M, Llorca J, Chan SC, Chiu W, Sheng PY, Yee A, Blackford MA, Pas SJ, Hill AJ, Alamgir FM. A Phenomenological Study of the Metal–Oxide Interface: The Role of Catalysis in Hydrogen Production from Renewable Resources. ChemSusChem 2008;1:905–10.
[11] Sun J, Qiu XP, Wu F, Zhu WT. H_2 from steam reforming of ethanol at low temperature over Ni/Y_2O_3, Ni/La_2O_3 and Ni/Al_2O_3 catalysts for fuel-cell application. Int J Hydrogen Energy 2005;30:437–45.
[12] Shanmugam V, Zapf R, Neuberg S, Hessel V, Kolb G. Effect of ceria and zirconia promotors on Ni/SBA-15 catalysts for coking and sintering resistant steam reforming of propylene glycol in microreactors. Appl Catal B Environ 2017;203:859–69.
[13] da Silva AAA, Bion N, Epron F, Baraka S, Fonseca FC, Rabelo-Neto RC, Mattos LV, Noronha FB. Effect of the type of ceria dopant on the performance of Ni/CeO_2 SOFC anode for ethanol internal reforming. Appl Catal B Environ 2017;206:626–41.
[14] Patel M, Jindal TK, Pant KK. Kinetic Study of Steam Reforming of Ethanol on Ni-Based Ceria−Zirconia Catalyst. Ind Eng Chem Res 2013;52:15763–71.
[15] Chen L, Chen F, Xia C. Direct synthesis of methane from CO_2–H_2O co-electrolysis in tubular solid oxide electrolysis cells. Energy Environ Sci 2014;7:4018–22.
[16] Hua B, Yan N, Li M, Zhang Y, Sun Y, Li J, Etsell Thomas, Sarkar Partha, Chuang Karl, Luo J-L. Novel layered solid oxide fuel cells with multiple-twinned $Ni_{0.8}Co_{0.2}$ nanoparticles: the key to thermally independent CO_2 utilization and power-chemical cogeneration. Energy Environ Sci 2016;9:207–15.
[17] Ni M. An electrochemical model for syngas production by co-electrolysis of H_2O and CO_2. J Power Sources 2012;202:209–16.
[18] Chen B, Xu H, Ni M. Modelling of SOEC-FT reactor: Pressure effects on methanation process. Appl Energy 2017;185:814–24.
[19] Chen B, Xu H, Ni M. Modelling of finger-like channelled anode support for SOFCs application. Sci Bull 2016;61:1324–32.
[20] Ni M, Leung MKH, Leung DYC. Electrochemical modeling of hydrogen production by proton-conducting solid oxide steam electrolyzer. Int J Hydrogen Energy 2008;33:4040–7.
[21] Chen B, Xu H, Zhang H, Tan P, Cai W, Ni M. A novel design of solid oxide electrolyser integrated with magnesium hydride bed for hydrogen generation and storage – A dynamic simulation study. Appl Energy 2017;200:260–72.
[22] He F, Song D, Peng R, Meng G, Yang S. Electrode performance and analysis of reversible solid oxide fuel cells with proton conducting electrolyte of $BaCe_{0.5}Zr_{0.3}Y_{0.2}O_{3-\delta}$. J Power Sources 2010;195:3359–64.
[23] Haberman BA, Young JB. Three-dimensional simulation of chemically reacting gas flows in the porous support structure of an integrated-planar solid oxide fuel cell. Int J Heat Mass Transf 2004;47:3617–29.
[24] Chen B, Xu H, Sun Q, Zhang H, Tan P, Cai W, He W, Ni, M. Syngas/power cogeneration from proton conducting solid oxide fuel cells assisted by dry methane reforming: A thermal-electrochemical modelling study. Energy Convers Manag 2018;167:37–44.
[25] Li M, Hua B, Luo J-L. Alternative Fuel Cell Technologies for Cogenerating Electrical Power and Syngas from Greenhouse Gases. ACS Energy Lett 2017;2:1789–96.

[26] Wang W, Su C, Ran R, Zhao B, Shao Z, O.Tade M, Liu S. Nickel-based anode with water storage capability to mitigate carbon deposition for direct ethanol solid oxide fuel cells. ChemSusChem 2014;7:1719–28.
[27] Nobrega SD, Galesco MV, Girona K, de Florio DZ, Steil MC, Georges S, Fonseca, FC. Direct ethanol solid oxide fuel cell operating in gradual internal reforming. J Power Sources 2012;213:156–9.
[28] Jiang Y, Virkar A V. A High Performance, Anode-Supported Solid Oxide Fuel Cell Operating on Direct Alcohol. J Electrochem Soc 2001;148:A706.
[29] Jiang SP, Ye Y, He T, Ho SB. Nanostructured palladium–$La_{0.75}Sr_{0.25}Cr_{0.5}Mn_{0.5}O_3/Y_2O_3$–$ZrO_2$ composite anodes for direct methane and ethanol solid oxide fuel cells. J Power Sources 2008;185:179–82.
[30] Steil MC, Nobrega SD, Georges S, Gelin P, Uhlenbruck S, Fonseca FC. Durable direct ethanol anode-supported solid oxide fuel cell. Appl Energy 2017;199:180–6.
[31] Cimenti M, Hill JM. Thermodynamic analysis of solid oxide fuel cells operated with methanol and ethanol under direct utilization, steam reforming, dry reforming or partial oxidation conditions. J Power Sources 2009;186:377–84.
[32] Akhairi MAF, Kamarudin SK. Catalysts in direct ethanol fuel cell (DEFC): An overview. Int J Hydrogen Energy 2016;41:4214–4228.
[33] Tan JL, De Jesus AM, Chua SL, Sanetuntikul J, Shanmugam S, Tongol BJV, Kim H. Preparation and characterization of palladium-nickel on graphene oxide support as anode catalyst for alkaline direct ethanol fuel cell. Appl Catal A Gen 2017;531:29–35.
[34] Zhiani M, Gasteiger HA, Piana M, Catanorchi S. Comparative study between platinum supported on carbon and non-noble metal cathode catalyst in alkaline direct ethanol fuel cell (ADEFC). Int J Hydrogen Energy 2011;36:5110–5116.
[35] Garcia AC, Linares JJ, Chatenet M, Ticianelli EA. $NiMnO_x$/C: A Non-noble Ethanol-Tolerant Catalyst for Oxygen Reduction in Alkaline Exchange Membrane DEFC. Electrocatalysis 2014;5:41–49.
[36] Bambagioni V, Bianchini C, Marchionni A, Filippi J, Vizza F, Teddy J, Serp P, Zhiani M. Pd and Pt-Ru anode electrocatalysts supported on multi-walled carbon nanotubes and their use in passive and active direct alcohol fuel cells with an anion-exchange membrane (alcohol=methanol, ethanol, glycerol). J Power Sources 2009;190:241–251.
[37] Hou H, Wang S, Jin W, Jiang Q, Sun L, Jiang L, Sun G. KOH modified Nafion112 membrane for high performance alkaline direct ethanol fuel cell. Int J Hydrogen Energy 2011;36:5104–5109.
[38] Modestov AD, Tarasevich MR, Leykin AY, Filimonov VY. MEA for alkaline direct ethanol fuel cell with alkali doped PBI membrane and non platinum electrodes. J Power Sources 2009;188:502–506.
[39] Li YS, Zhao TS, Liang ZX. Performance of alkaline electrolyte-membrane based direct ethanol fuel cells. J Power Sources 2009;187:387–392.
[40] Chen Y, Bellini M, Bevilacqua M, Fornasiero P, Lavacchi A, Miller HA, Wang L, Vizza F. Direct Alcohol Fuel Cells: Toward the Power Densities of Hydrogen-Fed Proton Exchange Membrane Fuel Cells. ChemSusChem 2015;8:524–533.
[41] Bambagioni V, Bianchini C, Chen Y, Filippi J, Fornasiero P, Innocenti M, Lavacchi A, Marchionni A, Oberhauser W, Vizza F. Energy efficiency enhancement of ethanol electrooxidation on Pd-CeO_2/C in passive and active polymer electrolyte-membrane fuel cells. ChemSusChem 2012;5:1266–1273.
[42] Osmieri L, Escudero-Cid R, Armandi M, Monteverde Videla AHA, García Fierro JL, Ocón P, Specchia S. Fe-N/C catalysts for oxygen reduction reaction supported on different carbonaceous materials. Performance in acidic and alkaline direct alcohol fuel cells. Appl Catal B Environ 2017;205:637–653.

[43] Osmieri L, Escudero-Cid R, Monteverde Videla AHA, Ocón P, Specchia S. Application of a non-noble Fe-N-C catalyst for oxygen reduction reaction in an alkaline direct ethanol fuel cell. Renew Energy 2018;115:226–237.
[44] Huang B, Wang SR, Liu RZ, Wen TL, Preparation and performance characterization of the Fe-Ni/ScSZ cermet anode for oxidation of ethanol fuel in SOFCs. J Power Sources 2007;167:288–294.
[45] Li Y, Wong LM, Xie H, Wang S, Su PC. Nanoporous palladium anode for direct ethanol solid oxide fuel cells with nanoscale proton-conducting ceramic electrolyte. J Power Sources 2017;340:98–103.
[46] Liao M, Wang W, Ran R, Shao Z. Development of a Ni–$Ce_{0.8}Zr_{0.2}O_2$ catalyst for solid oxide fuel cells operating on ethanol through internal reforming. J Power Sources 2011;196:6177–6185.
[47] Lo Faro M, Reis RM, Saglietti GGA, Oliveira VL, Zignani SC, Trocino S, Maisano S, Ticianelli EA, Hodnik N, Ruiz-Zepeda F, Aricò AS. Solid oxide fuel cells fed with dry ethanol: The effect of a perovskite protective anodic layer containing dispersed Ni-alloy@FeOx core-shell nanoparticles. Appl Catal B Environ 2018;220:98–110.
[48] Lo Faro M, Reis R.M, Saglietti GGA, Zignani SC, Trocino S, Frontera P, Antonucci PL, Ticianelli EA, Aricò AS. Investigation of Ni-based alloy/CGO electro-catalysts as protective layer for a solid oxide fuel cell anode fed with ethanol. J Appl Electrochem 2015;45:647–656.
[49] Mat MD, Liu X, Zhu Z, Zhu B. Development of cathodes for methanol and ethanol fuelled low temperature (300-600°C) solid oxide fuel cells. Int J Hydrogen Energy 2007;32:796–801.
[50] Morales M, Espiell F, Segarra M. Improvement of performance in low temperature solid oxide fuel cells operated on ethanol and air mixtures using Cu-ZnO-Al_2O_3catalyst layer, J Power Sources 2015;293:366–372.
[51] Sarruf BJM, Hong JE, Steinberger-Wilckens R, de Miranda PEV, CeO_2–Co_3O_4–CuO anode for direct utilisation of methane or ethanol in solid oxide fuel cells. Int J Hydrogen Energy 2018;43:6340–6351.
[52] Sumi H, Yamaguchi T, Shimada H, Fujishiro Y, Awano M, Internal partial oxidation reforming of butane and steam reforming of ethanol for anode-supported microtubular Solid Oxide Fuel Cells. Fuel Cells 2017;17:875–881.
[53] Tao Z, Hou G, Xu N, Zhang Q, A highly coking-resistant solid oxide fuel cell with a nickel doped ceria: $Ce_{1-x}Ni_xO_2$-yreformation layer. Int J Hydrogen Energy 2014;39:5113–5120.
[54] Ullah MK, Raza R, Asghar MI, Ali A, Rafique A, Abbas G, Ahmad MA, Hanif I, Akbar M, Lund PD. Tri-doped ceria ($M_{0.2}Ce_{0.8}O_{2-\delta}$, M= $Sm_{0.1}Ca_{0.05}Gd_{0.05}$) electrolyte for hydrogen and ethanol-based fuel cells. J Alloys Compd 2019;773:548–554.
[55] Wang W, Chen Y, Wang F, O.Tade M, Shao Z. Enhanced electrochemical performance, water storage capability and coking resistance of a $Ni^{+}BaZr_{0.1}Ce_{0.7}Y_{0.1}Yb_{0.1}O_{3-\delta}$ anode for solid oxide fuel cells operating on ethanol. Chem Eng Sci 2015:;126:22–31.
[56] Wang W, Su C, Zheng T, Liao M, Shao Z. Nickel zirconia cerate cermet for catalytic partial oxidation of ethanol in a solid oxide fuel cell system. Int J Hydrogen Energy 2012;37:8603–8612.
[57] Wang W, Wang F, Ran R, Park HJ, Jung DW, Kwak C, Shao Z. Coking suppression in solid oxide fuel cells operating on ethanol by applying pyridine as fuel additive. J Power Sources 2014;265:20–29.
[58] Ye XF, Huang B, Wang SR, Wang ZR, Xiong L, Wen TL. Preparation and performance of a Cu-CeO_2-ScSZ composite anode for SOFCs running on ethanol fuel. J Power Sources 2007;164:203–209.

[59] Ye XF, Wang SR, Hu Q, Chen JY, Wen TL, Wen ZY. Improvement of Cu-CeO_2 anodes for SOFCs running on ethanol fuels. Solid State Ionics 2009;180:276–281.
[60] Ye XF, Zhou J, Wang SR, Zeng FR, Wen TL, Zhan ZL. Research of carbon deposition formation and judgment in Cu-CeO_2-ScSZ anodes for direct ethanol solid oxide fuel cells. Int J Hydrogen Energy 2012;37:505–510.

Figures

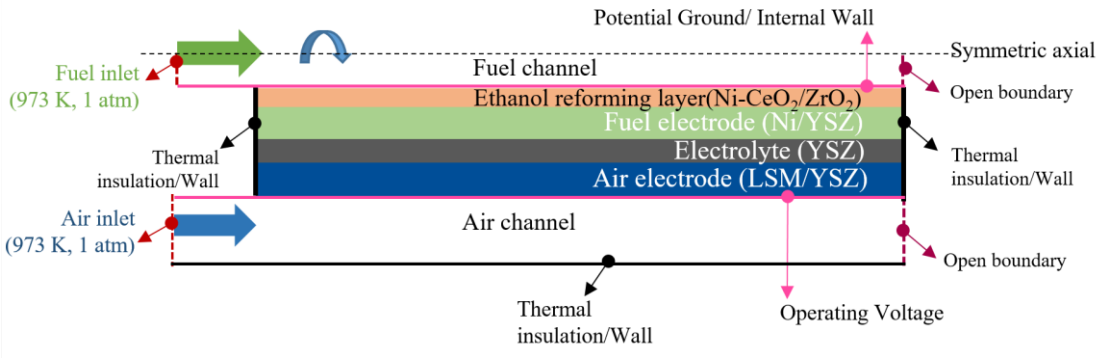

Fig. 1. Schematic of the axial symmetry model of the tubular ethanol-fuelled SOFC with boundary conditions.

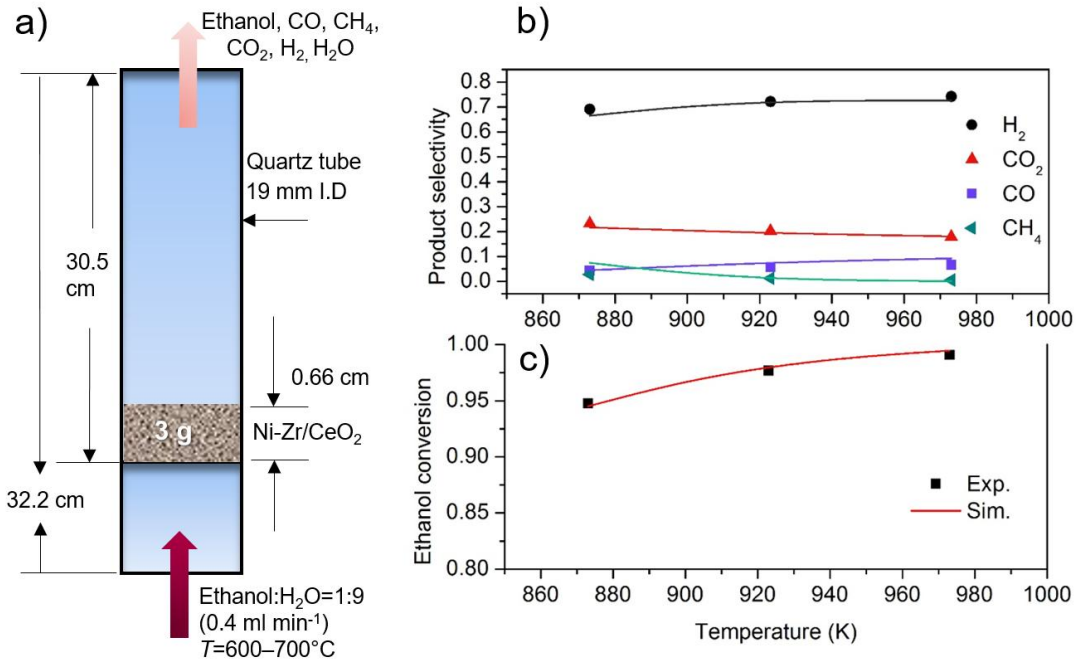

Fig. 2. The fixed-bed reactor for catalyst kinetics measurement and validation: (a) operating conditions and dimensions of the reactor; (b) comparison of the experimental vs. simulated species selectivity; (c) the ethanol conversion ratio.

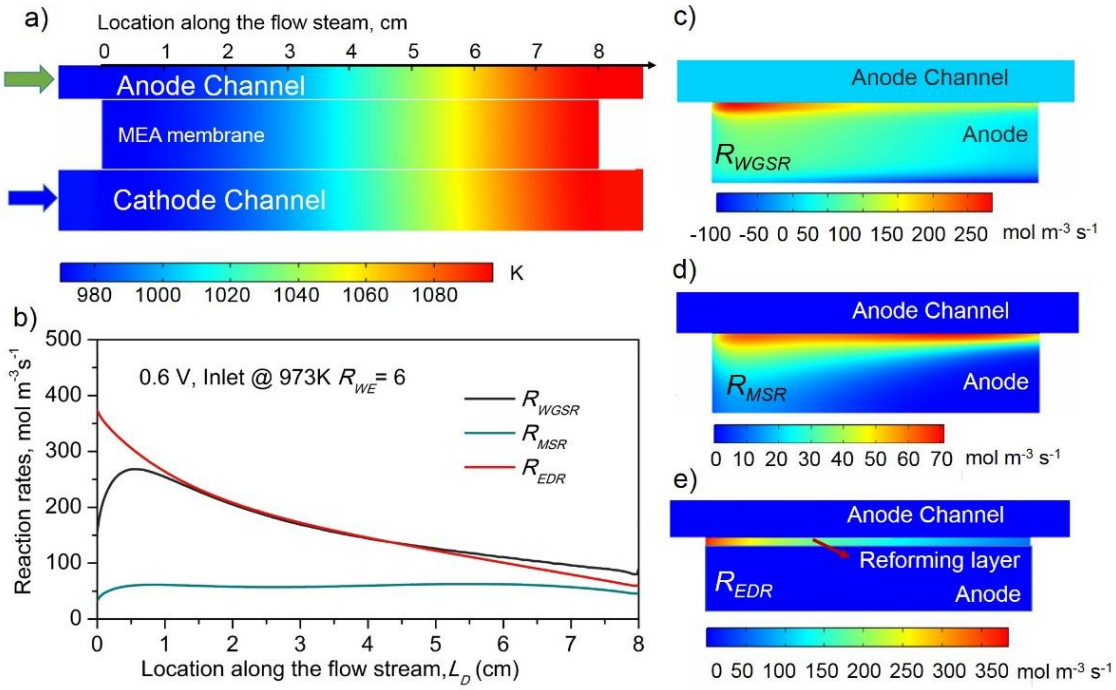

Fig. 3. The base case simulated results of reforming reactions: (a) temperature distribution of the gas channels and MEA (anode, electrolyte and cathode); (b) the reaction rates of water gas shifting R_{WGSR}, methane steam reforming R_{MSR} and ethanol steam reforming R_{ESR} at the middle of ethanol reforming layer; (c−e) their distribution in the anode (adjacent to the anode channel signed by 0).

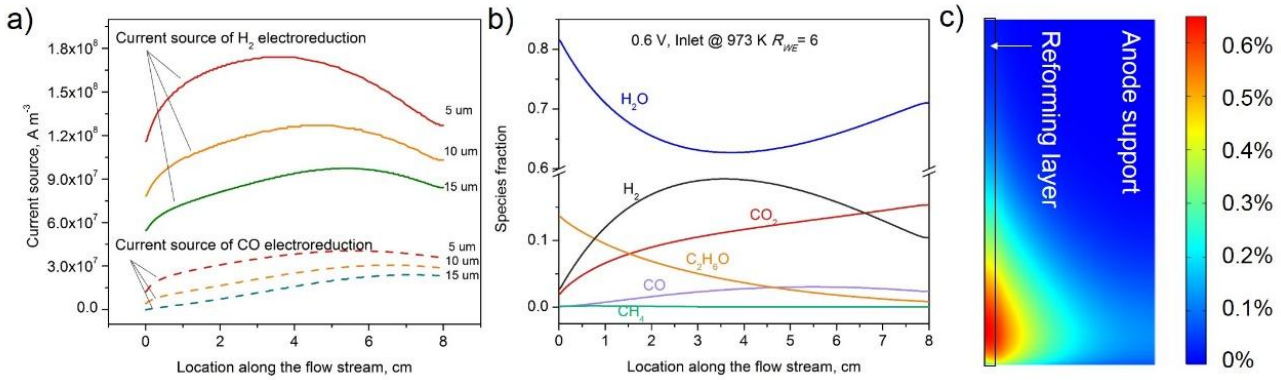

Fig. 4. (a) The current source distribution at different anode location of d=5; 10; 15 μm to the anode-electrolyte interface; (b) The species fraction along the flow stream at the anode-electrolyte interface. (c) CH_4 fraction distribution in the reforming layer and anode support layer.

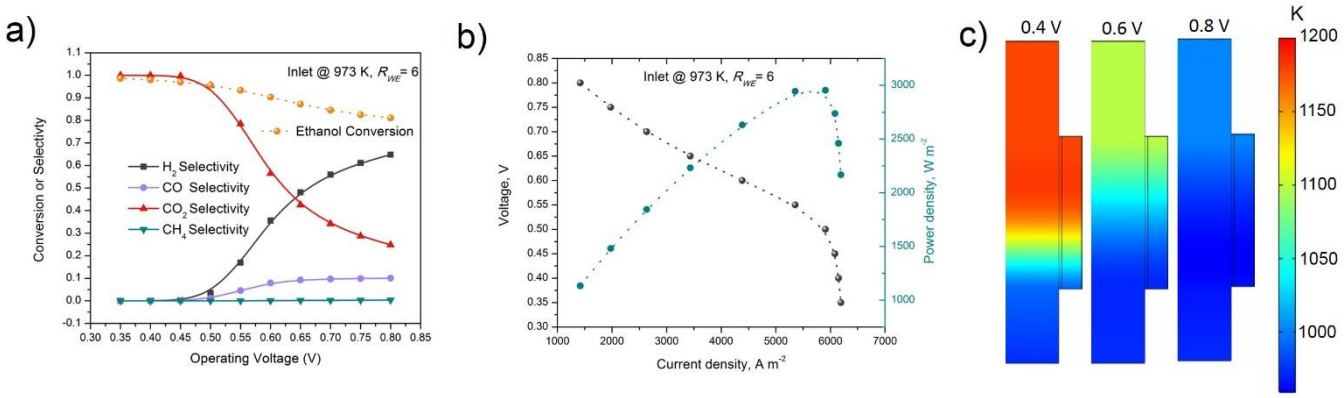

Fig. 5. (a) Ethanol conversion and species selectivity at the outlet at different operating voltage (0.35−0.8 V) with inlet temperature at 973 K; (b) the voltage/power-current curves of the E-SOFC; (c) the temperature distribution at 0.4, 0.6 and 0.8 V of the anode channel and anodic reforming layer and support layer).

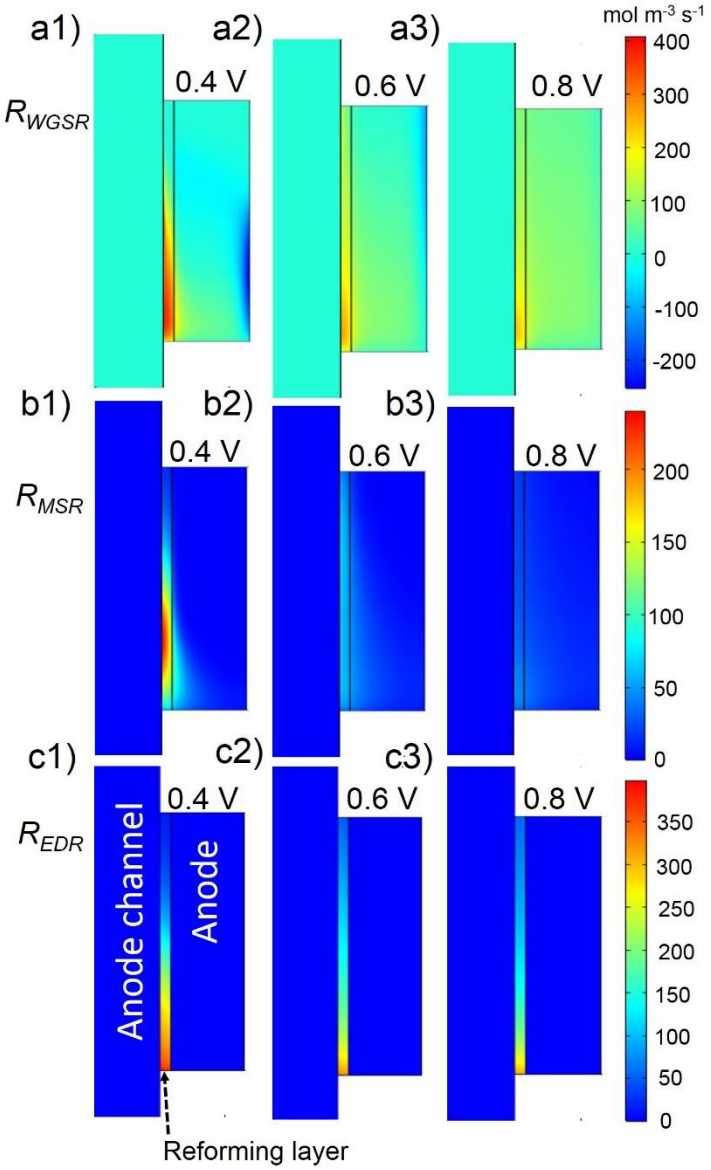

Fig. 6. The reaction rates distribution in anodic reforming layer and anode support layer at 0.4; 0.6 and 0.8 V: (a1−a3) R_{WGSR}; (b1−b3) R_{MSR}; (c1−c3) R_{ESR}.

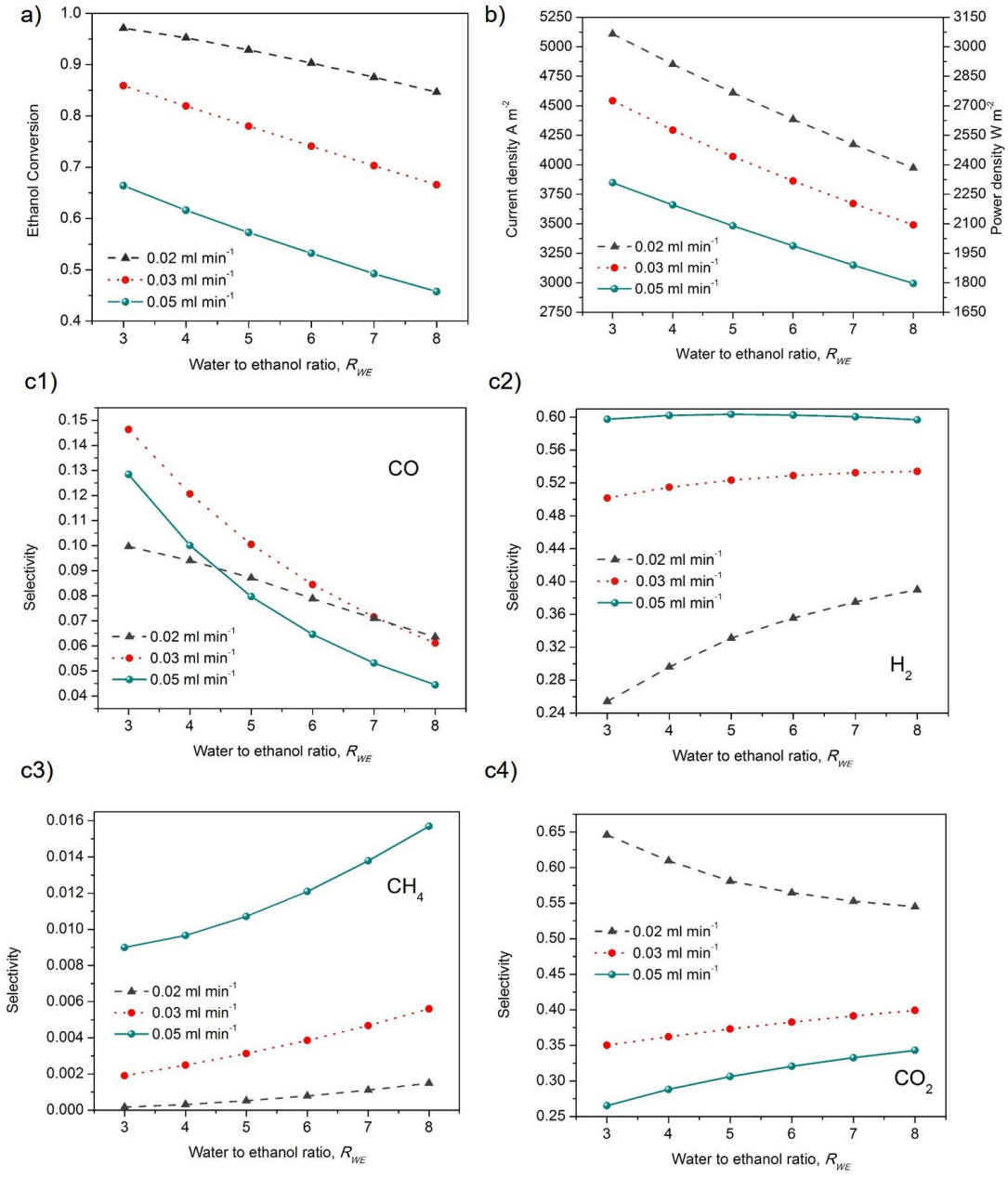

Fig. 7. Effects of water to ethanol ratio R_{WE} at 0.6 V with ethanol feeding varied from 0.02 ml min^{-1} to 0.05 ml min^{-1}: (a) simulated ethanol conversion ratio; (b) the current and power density of the SOFC; (c1−c4) the outlet species selectivity of CO, H_2, CH_4 and CO_2.

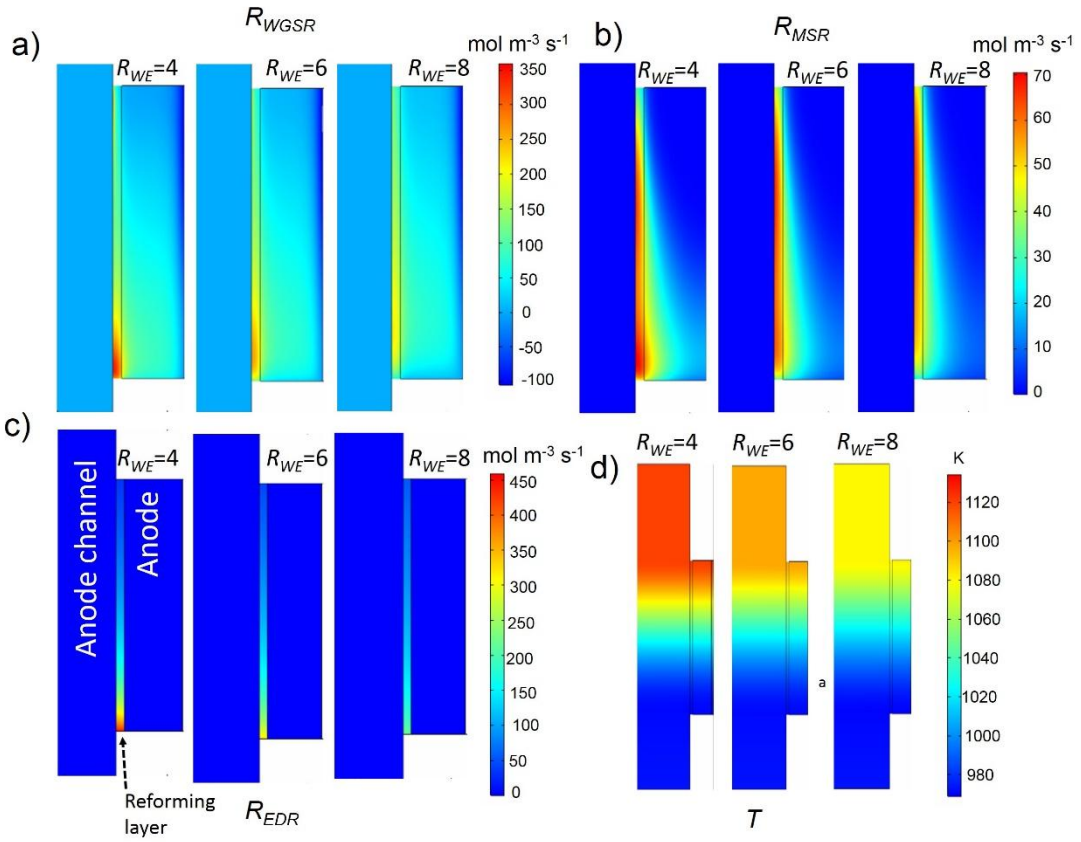

Fig. 8. The reaction rates distribution in anodic reforming layer and anode support layer at different water to ethanol ratio (R_{WE}=4, 6 and 8): (a1−a3) R_{WGSR}; (b1−b3) R_{MSR}; (c1−c3) R_{ESR} and (d) temperature distribution.

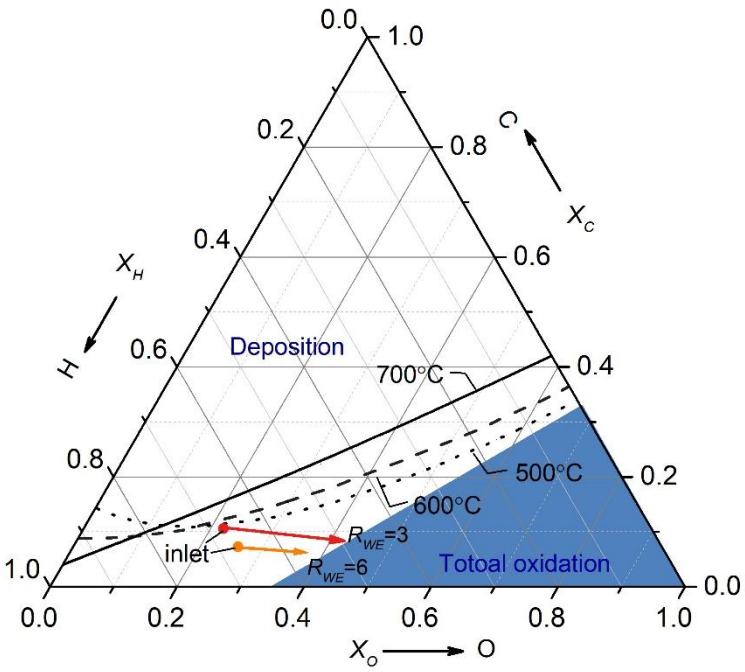

Fig. 9. The ternary diagram of O, C and H elements of the gas mixture with regions of depositions and total oxidation of carbon based on thermodynamic equilibrium. The composition trajectories of R_{WE}=3 and 6 operating shown by the red line and orange arrow along the flow direction at the midline of reforming layer.

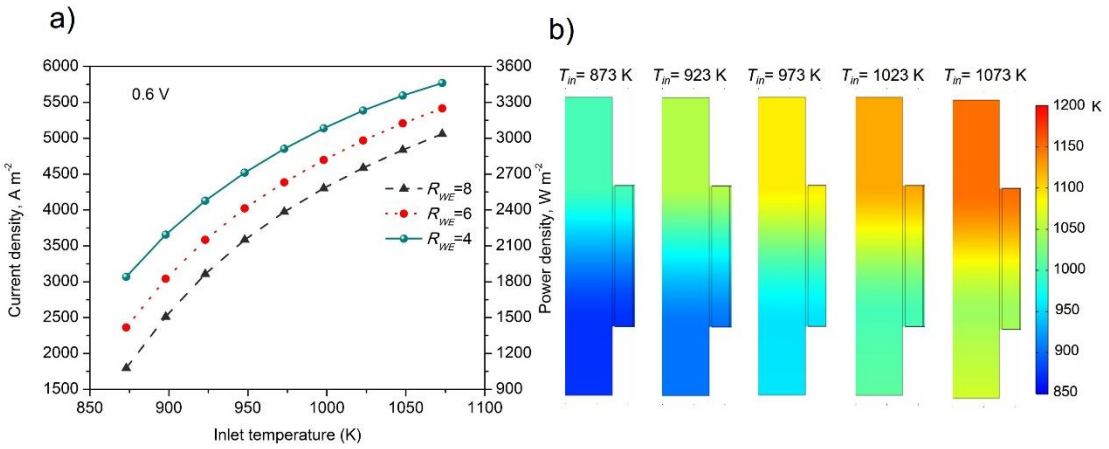

Fig. 10. (a) The current and power density of the SOFC (0.6 V operating) at varied inlet gas temeprature at different R_{WE}; (b) the affected temperature distribution of the anode side with R_{WE}=6, 0.6 V.

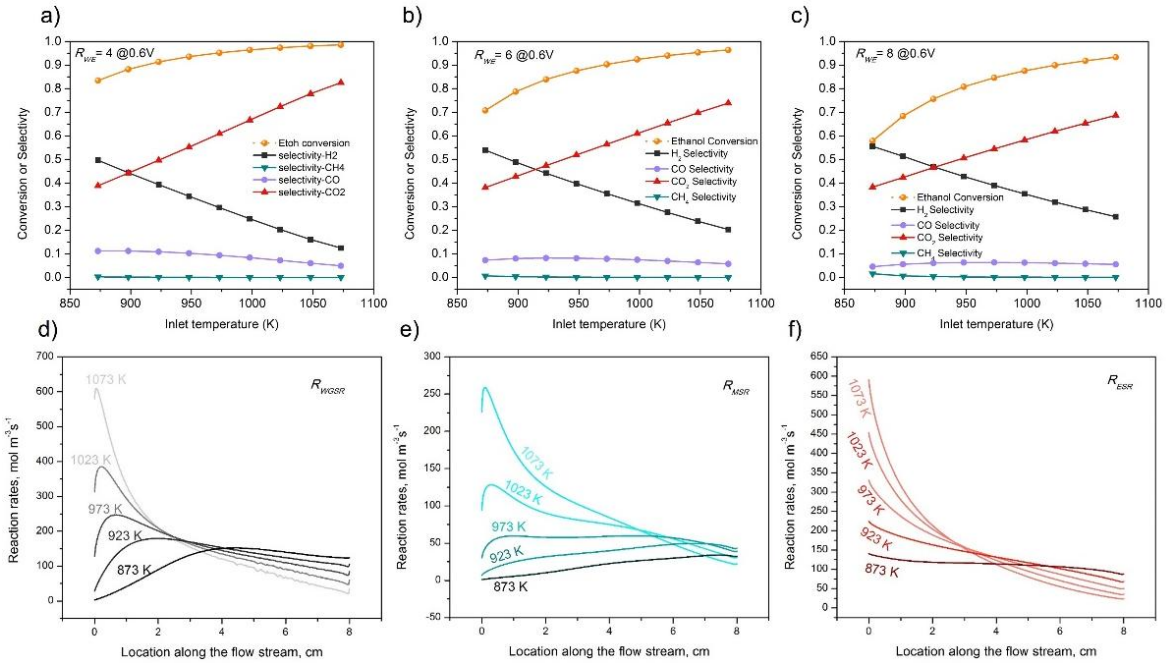

Fig. 11. The ethanol conversion and species selectivity at the SOFC outlet with varied inlet gas temperature (873 K to 1073 K) at (a) R_{WE} =4 (b) R_{WE} =6 (c) R_{WE} =8; (d−f) the corresponding reaction rates R_{WGSR}, R_{MSR} and R_{MSR} at the mid of the ethanol reforming layer at R_{WE}=6.

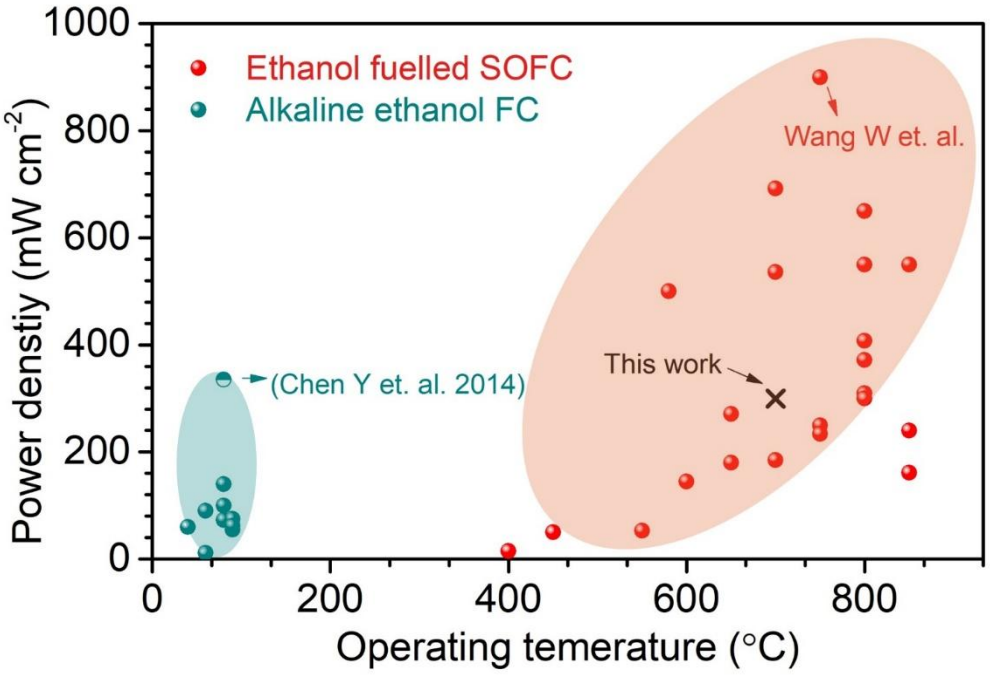

Fig. 12. The power densities of state-of-art alkaline ethanol fuel cells and ethanol fuelled SOFCs [34,37−64].

Tables

Table 1 Dimensions and basic operating parameters of E-SOFC [18–20].

Parameters	Values
Cell length	8 cm
Inner radius	0.175 cm
Porosity of Electrodes	0.4
Tortuosity of Electrodes	2
30%wt Ni-ZrO_2/CeO_2 reforming layer	60 μm
Ni-YSZ anode support	310 μm
Electrolyte	12 μm
LSM Cathode electrode	30 μm
Operating voltage	0.6 V
Operating Pressure	1 atm
Inlet temperature	973 K
Inlet fuel mole ratio, R_{WE}	Water steam:ethanol = 6:1
Inlet ethanol flow rate	0.02 ml min^{-1} at STP
Air flow	3 times stoichiometry

Table 2 Catalyst kinetic characterization fixed-bed reactor specification.

Parameters	Value
Bed height	0.66 cm
Radius	19 mm i.d.
Catalyst mass	3 g (diluted by 6 g silicon carbide)
Porosity	0.55
Feeding water to ethanol molar ratio, R_{WE}	9:1
Flow rate of ethanol	0.4 mL min^{-1} (std)
Temperature	600−700°C

Table 3 Boundary conditions for E-SOFC.

Processes	Anode inlet	Cathode inlet	Outlets
Mass transfer	$x_{H2O} = R_{WE}/(R_{WE}+1)$ $x_{Etoh} = 1/(R_{WE}+1)$ $x_{others} = 0$	$x_{O2} = 0.21$ $x_{N2} = 0.79$	Free flow condition
Momentum transfer	Constant velocity (flow rate)	Constant velocity (flow rate)	*P*=1 atm
Energy transfer	*T*=973 K	*T*=973K	$-\mathbf{n}\cdot\mathbf{q} = 0$

Table 4 Summary of base case results.

Parameters	Value
Ethanol conversion	0.903
H_2 selectivity	0.357
Outlet composition in volume C_2H_5OH:CO:CO_2:CH_4:H_2O:H_2	0.91% : 2.08% : 14.88% : 0.02% : 72.75% : 9.37%
Average current density	4385.6 A m^{-2}
Output electricity power density	2631.4 W m^{-2}